Scripta Materialia 274 (2026) 117115

Contents lists available at ScienceDirect

Scripta Materialia

journal homepage: www.journals.elsevier.com/scripta-materialia

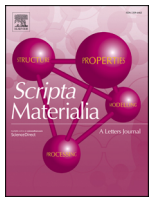

# Two-step deep learning for decoding elastic constants of hexagonal-symmetry materials from resonant-spectrum image

Kazuya Kohira [a], Shota Nakamura [a], Hiroki Fukuda [a], Kazuhiro Kyotani [b], Hirotsugu Ogi [a,*]

[a] The University of Osaka, Yamadaoka 2-1, Suita, 565-0871, Osaka, Japan
[b] Insight K. K., 2-6-7 Hyakunincho, Shinjuku-ku, 169-0073, Tokyo, Japan

ARTICLE INFO

*Keywords:*
Elastic constants
Hexagonal
Deep learning
Resonant ultrasound spectroscopy
Elasticity image
Average Young's modulus

ABSTRACT

We developed a deep learning (DL) framework based on convolutional neural networks (CNNs) to predict elastic constants of hexagonal materials by leveraging high image-recognition capability of CNNs. Resonant frequency data were converted into three-channel RGB images, referred to as "elasticity images" for CNN training. Without mode identification, the trained models accurately predicted all five independent elastic constants. We reveal that the average Young modulus is a critical for classification of hexagonal materials based on their elasticity images. Furthermore, we extended the Blackman diagram, originally developed for cubic crystals, to hexagonal systems, enabling a substantial reduction of five-dimensional elastic-constant space. We then established a two-step DL scheme: first, classification using the average Young modulus, followed by regression of the five elastic constants in the classified average-Young-modulus class. The prediction error was approximately 5 % for the principal elastic constants and 1.5 % for the average Young modulus.

Elastic constants are fundamental physical quantities that govern the deformation behavior of materials under external forces. They are indispensable for the design and analysis of structures and devices in various engineering applications. Furthermore, since elastic constants strongly reflect interatomic potentials, they serve as crucial benchmarks for validating the value obtained from theoretical models, such as density-functional-theory calculations [1–6]. Consequently, the accurate measurement of elastic constants is of great importance both in scientific studies and practical applications.

In particular, the measurement of elastic constants in hexagonal crystal systems is of high significance. For example, gallium nitride (GaN) and silicon carbide (SiC), which have garnered attention as power semiconductor materials, belong to the hexagonal system [7,8]. Moreover, even lower-symmetry materials and composite materials can often be approximated with sufficient accuracy as hexagonal materials in practical applications. For instance, unidirectionally fiber-reinforced composites [9], which are important engineering materials because of their high stiffness and toughness, lotus-type porous metals [10,11] with lightweight and high energy absorption capacity, and biological bone tissues [12] exhibit hexagonal symmetry on a macroscopic scale [13–16]. Due to the prevalence of such materials, establishment of a technique for determining the elastic constants of hexagonal materials remains a central issue in the materials science field.

Conventional ultrasonic techniques such as the pulse-echo method [17] and resonance method [18,19] have long been used for the elastic-constant measurements. However, in materials with low symmetry, where the number of independent elastic constants is large, these techniques require specimens cut along multiple crystallographic orientations, which is challenging for small samples.

To overcome these limitations, the resonance-ultrasound-spectroscopy (RUS) method has been developed [20–27]. This technique enables the determination of all independent elastic constants from a single small specimen by measuring many free-vibration resonance frequencies and fitting the calculated resonance frequencies to them through inverse calculation. However, a major drawback of the RUS method lies in the difficulty of mode identification. If the correspondence between measured and theoretical resonance modes is incorrect during the inverse process, the resultant elastic constants are physically meaningless. To avoid this problem, it is generally needed to calculate the resonance frequencies that closely match the corresponding experiments in the inverse calculation, meaning a

* Corresponding author. ogi@prec.eng.osaka-u.ac.jp.
*E-mail addresses:* kohira@qm.prec.eng.osaka-u.ac.jp (K. Kohira), nakamura@qm.prec.eng.osaka-u.ac.jp (S. Nakamura), h.fukuda@qm.prec.eng.osaka-u.ac.jp (H. Fukuda), kazuhiro-kyotani@insightkk.co.jp (K. Kyotani), ogi@prec.eng.osaka-u.ac.jp (H. Ogi).

https://doi.org/10.1016/j.scriptamat.2025.117115
Received 5 September 2025; Accepted 21 November 2025
Available online 3 December 2025

contradiction in that prior knowledge of the elastic constants close to the true values are required.

To address this issue, a variety of strategies have been proposed [21,25,26]. For example, mode selective excitation and detection were performed using electromagnetic acoustic transducers by controlling the direction of the magnetic field [28,29], and the vibrational mode figure was measured at each resonance using laser Doppler interferometry to achieve complete mode identification [30–32]. However, these methods require sophisticated experimental setups and expert-level understanding in acoustics and materials-science fields, limiting their accessibility. Alternative approaches such as using Bayesian estimation [33] have also been proposed; however, even in these methods, the dependence on initial values becomes more pronounced as the crystal symmetry decreases.

Recently, convolutional neural networks (CNNs) have drawn attention for their superior ability in image-based classification and regression tasks. CNNs are capable of learning local feature representations from input image without manual intervention. Leveraging this image recognition capability, various studies have utilized CNNs to analyze data structured in two-dimensional formats [34–36]. Based on this, we proposed a novel elastic-constant prediction method utilizing CNNs [37], where we converted the mechanical resonance spectra into the elasticity images and trained originally developed CNNs with them with corresponding elastic constants, resulting in the prediction of the elastic constants of cubic materials with ~10 % errors without mode identification and inverse calculation. In that study, the Blackman diagram – a plot of $C_{12}/C_{11}$ against $C_{44}/C_{11}$, graphically categorizing the elastic properties of cubic materials [38,39]– was necessary to constrain the range of the dataset, which reduced the dataset size by 60 % and contributed to improved prediction accuracy [37]. However, extending this approach to hexagonal systems presents further difficult challenges. Due to the five-dimensional space of independent elastic constants in hexagonal symmetry, the network has to be trained with a vast dataset to accurately predict all five constants simultaneously, which is computationally demanding task and difficult to optimize for high accuracy. Furthermore, unlike the cubic case, no diagram analogous to the Blackman diagram exists for hexagonal crystals. Consequently, it is not possible to restrict the dataset range, and with two additional variables compared to the cubic case, the number of required data points can easily exceed one hundred million.

Motivated by this challenge, we focus on the average Young modulus ($E_{\mathrm{Ave}}$), the Young modulus of an isotropic solid that is elastically averaged in all directions for the anisotropic solid, because we find it to be the most strongly encoded physical quantity in the elasticity image. Based on $E_{\mathrm{Ave}}$, we find Blackmann-diagram like relationships for hexagonal systems and succeed in significantly reducing the elastic-constant ranges to be examined. We thus propose a two-step prediction method: First is the classification scheme based on $E_{\mathrm{Ave}}$, which effectively narrows down the candidate range of the dataset, and second is the regression process for the five elastic constants around the predicted $E_{\mathrm{Ave}}$ as a constraint. This method allows for the prediction of the elastic constants of hexagonal materials without mode identification and inverse calculation even missing modes are involved. We demonstrate that the prediction errors of the main elastic constants can be suppressed to ~5 %, confirming the effectiveness of our approach.

The elastic-constant matrix $C_{ij}$ for hexagonal systems is generally expressed with the five independent elastic constants $C_{11}, C_{12}, C_{13}, C_{33}$, and $C_{44}$ as:

$$[C_{ij}] = \begin{bmatrix} C_{11} & C_{12} & C_{13} & 0 & 0 & 0 \\ & C_{11} & C_{13} & 0 & 0 & 0 \\ & & C_{33} & 0 & 0 & 0 \\ & & & C_{44} & 0 & 0 \\ & sym. & & & C_{44} & 0 \\ & & & & & \frac{C_{11}-C_{12}}{2} \end{bmatrix} \quad (1)$$

In the RUS method, a rectangular parallelepiped specimen with edges parallel to the three crystallographic axes is prepared for determining the $C_{ij}$. In this study, we consider rectangular parallelepiped specimens with the side-length ratio of 5:3:4, where the edge with the intermediate length (ratio = 4) is aligned with the $c$-axis. Restricting the specimen shape to this dimensional ratio is not usually a problem in the RUS method, because the RUS method anyway requires cutting a specimen from the sample, which can be prepared according to this dimensional ratio. Furthermore, our previous study indicates that deviation from this edge ratio insignificantly affects the prediction accuracy [37].

Using the Ritz method for Hamilton's principle, the resonant frequencies are calculated by solving an eigenvalue problem [21]

$$\left(\mathbf{\Gamma} - \rho\omega^2\mathbf{I}\right)\mathbf{u} = 0, \quad (2)$$

where $\mathbf{I}$ denotes the unit matrix, $\rho$ is the mass density, $\omega$ is the angular frequency, and $\mathbf{u}$ is the vector made of coefficients of basis functions for displacements. The components of the matrix $\mathbf{\Gamma}$ are determined by the elastic constants and dimensions of the specimen, and they are inversely proportional to a product of two side-length dimensions. Because the side-length ratio is maintained, the matrix $\mathbf{\Gamma}$ can be represented by $\tilde{V}^{-\frac{2}{3}}\mathbf{\Gamma_R}$ with that for the reference specimen, $\mathbf{\Gamma_R}$. Here, $\tilde{V}$ denotes the volume ratio of the specimen to the reference specimen with side lengths of 5 mm, 3 mm, and 4 mm. Therefore, Eq. (2) can be rewritten as

$$\left(\mathbf{\Gamma_R} - \tilde{V}^{\frac{2}{3}}\rho\omega^2\mathbf{I}\right)\mathbf{u} = \left(\mathbf{\Gamma_R} - \tilde{C}\mathbf{I}\right)\mathbf{u} = 0. \quad (3)$$

Note that $\tilde{C}$ indicates the common eigenvalue independent of mass density and volume (or $\tilde{V}$) of the specimen, purely reflecting the elastic property of the material. We thus introduce the elasticity parameter $\tilde{C}_n$ given by

$$\tilde{C}_n = 4\pi^2\tilde{V}^{\frac{2}{3}}\rho f_n^2, \quad (4)$$

where $f_n$ is the $n$th resonance frequency.

Fig. 1 shows an overview of the elastic-constant determination with deep learning proposed in this study. The resonant spectrum obtained by, for example, the tripod piezoelectric transducers [30] (Fig. 1(a)) gives numerous number of resonant frequencies, and using the first 100 frequencies, we create the elasticity image composed of three binary images by converting the resonant frequencies into the elasticity parameters in Eq. (4) as follows.

We set minimum and maximum boundaries for $\tilde{C}_n$ to be 3950 and 592,500 TPa·m$^{-2}$, respectively, between which the 100 elasticity parameters of most specimens are expected to be included, although some higher modes of very stiff materials exceed the maximum boundary and are excluded in the elasticity image. For example, for titanium with the reference dimensions, the lower and upper limits of $\tilde{C}_n$ correspond to the resonant frequencies of 0.149 MHz and 1.82 MHz, respectively, where the fundamental mode (0.264 MHz) and the 100th mode (1.35 MHz) are included.

The $\tilde{C}_n$ values are mapped onto a $30 \times 30$ pixel grid by dividing the $\tilde{C}_n$ range into 900 equal intervals and recording the binary presence (1) or absence (0) of a resonance mode in each interval (Fig. 1(b)). The three binary layers are generated using different mapping strategies as shown in Fig. 1(c): (i) The red layer assigns values spirally from the center outward, (ii) the green layer maps values spirally from the outer edge inward, and (iii) the blue layer maps values raster-wise from top to bottom. These layers are combined into a single RGB image representing the material's elastic behavior (Fig. 1(d)). For instance, as shown in Fig. 1(e), softer materials tend to produce localized, non-overlapping pixel patterns, whereas stiffer materials generate more distributed and overlapping patterns across layers. These spatial characteristics are effectively learned by our CNNs.

We have successfully reduced the dataset size by referring the Blackman diagram [37], which plots the ratio of elastic constants $C_{44}/C_{11}$ on the horizontal axis and $C_{12}/C_{11}$ on the vertical axis; it has been used to discuss the elastic properties of cubic crystals [38,39]. However, the Blackman diagram is proposed for cubic materials, and it is unavailable for hexagonal systems.

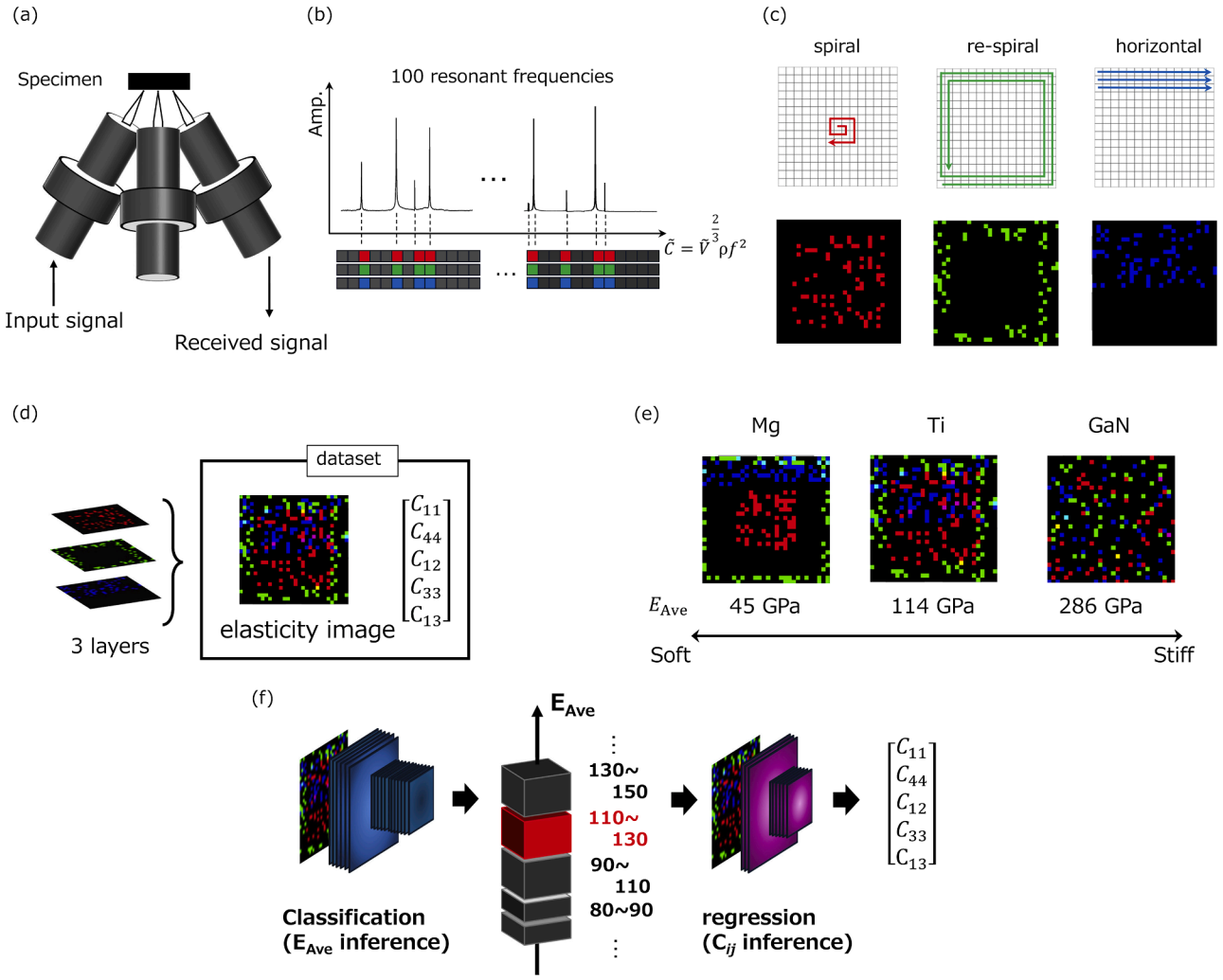


**Fig. 1.** Schematic diagram of deep learning scheme we propose. (a) RUS experimental setup with needle-llike tripod transducers. (b) Conversion of resonant frequencies into elasticity parameters. (c) Three methods for distributing 900 elastic parameters within 30x30 pixels. (d) Construction of the elasticity image and dataset. (e) Elasticity images for three hexagonal materials with different average Young modulus $E_{Ave}$. (f) The two-step deep-learning scheme for predicting the five independent elastic constants.

We then extend the concept of the Blackman diagram to hexagonal systems in order to constrain the range of elastic constants in our dataset. In implementing this, we find that the average Young modulus $E_{Ave}$ is a key factor as discussed later and, therefore, adopt this instead of $C_{11}$, because $E_{Ave}$ is highly dependent on $C_{11}$ as shown in Fig. 2(a). Thus, we select $E_{Ave}$, $C_{33}$, $C_{12}$, $C_{13}$, and $C_{44}$ as the five elastic constants of hexagonal systems for preparing the elasticity images. (Note that $C_{11}$ can be calculated from these five elastic constants.)

The Blackman diagram shows a relationship between the shear modulus ($C_{44}$) and the off-diagonal modulus ($C_{12}$) normalized by the longitudinal-wave modulus (or the largest modulus) ($C_{11}$) for a cubic crystal. In hexagonal systems, there are two longitudinal-wave moduli ($C_{11}$ and $C_{33}$), but we use $C_{33}$ because of its high independency from the average Young modulus (Fig. 2(a)).

Based on reported elastic constants for 42 existing hexagonal materials (see Table S1 in Supplementary Information), we find that the range of values that the ratio $C_{33}/E_{Ave}$ can take is narrow, distributed between 0.6 and 2.1, and we divided this range into three regions at 0.5 intervals as shown in Fig. 2(b). We then constructed the relationships between the normalized shear modulus ($C_{44}/C_{33}$) and the normalized off-diagonal moduli ($C_{12}/C_{33}$ and $C_{13}/C_{33}$) for the three regions in Fig. 2(c)–(e). We refer to these diagrams as the hexagonal Blackmann diagrams (hBDs). Interestingly, although $C_{12}$, $C_{13}$, $C_{33}$, and $C_{44}$ are independent, existing materials show characteristic distributions on hBDs. For example, in materials where $C_{33}/E_{Ave}$ is relatively small, the plots tend to be distributed over a wide range on the left side, whereas in materials with larger $C_{33}/E_{Ave}$ values, the plots appear in localized areas. This finding indicates that the degrees of freedom in the elastic-constant space can be dramatically reduced. We considered the elastic-constant spaces colored in Fig. 2(b)–(e) and used them to create the elasticity-image dataset.

Fig. 1(f) explains the two-step DL method we propose for determining the five independent elastic constants of hexagonal systems. First, we classified hexagonal symmetry materials into 15 classes based on their $E_{Ave}$ values. The considered range for the average Young modulus was 40–470 GPa, based on the values of the existing materials. This range was divided into 15 classes as follows: The range of 40–90 GPa was divided into five classes at 10 GPa intervals, the range of 90–190 GPa was into five classes at 20 GPa intervals, the range of 190–270 GPa was into two classes at 40 GPa intervals, the range of 270–390 GPa was into two classes at 60 GPa intervals, and the range of 390–470 GPa was classified as one class. (As $E_{Ave}$ increases, the width of each class becomes larger to ensure uniform sampling.)

For each class, we randomly selected 792,000 sets of the five elastic-constant parameters ($E_{Ave}$, $C_{33}/E_{Ave}$, $C_{12}/C_{33}$, $C_{13}/C_{33}$, and $C_{44}/C_{33}$) within the reduced elastic-constant space and constructed the

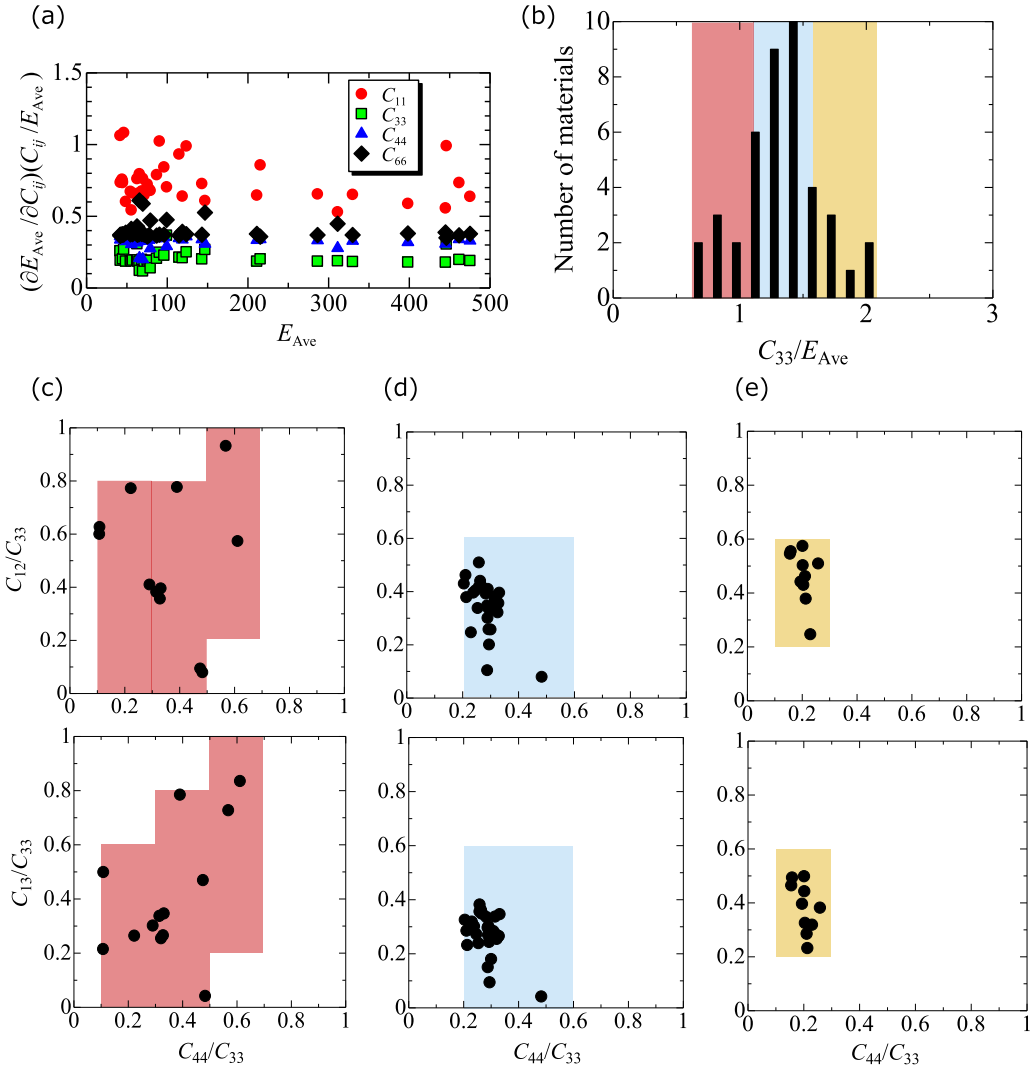


**Fig. 2.** (a) Sensitivity of the average Young modulus to principal elastic constants for 42 existing materials shown in Table S1. (b) A histgram of the ratio between $C_{33}$ and $E_{Ave}$ for the reported 42 hexagonal materials in Table S1. The distribution is divided into three regions shown with red (0.6-1.1), light blue (1.1-1.6), and light yellow (1.6-2.1); and hexagonal Blackman diagrams for $C_{12}$ (upper) and $C_{13}$ (lower) in the three ranges of $C_{33}/E_{Ave}$ of (c)0.6-1.1, (d)1.1-1.6, and (e)1.6-2.1.

corresponding elasticity images. For example, in the class of $E_{Ave}$ of 110–130 GPa, we consider three spaces defined by (i)110< $E_{Ave}$ <130, 0.6< $C_{33}/E_{Ave}$ <1.1, and red region in Fig. 2(c), (ii)110< $E_{Ave}$ <130, 1.1< $C_{33}/E_{Ave}$ <1.6, and light-blue region in Fig. 2(d), and (iii)110< $E_{Ave}$ <130, 1.6< $C_{33}/E_{Ave}$ <2.1, and light-yellow region in Fig. 2(e), and randomly selected 528,000, 216,000, and 48,000 points in five-dimensional spaces (i), (ii), and (iii), respectively, so as to maintain nearly the same sampling-point density. Furthermore, to enhance robustness against missing modes, 0 to 5 resonance modes were randomly omitted from the resonance spectra in the training data.

In the second step, we predicted the five elastic constants using the dataset in the class identified by the first step. This two-step strategy highly contributes to accurately decoding the elastic constants because of significantly narrowed range of the dataset to be used in the regression stage.

For the first classification step, we adopted the 192-layer CNN architecture as shown in Supplementary Figure S1. The network takes a 30×30 three-layer elasticity image as an input and begins with a 2D convolutional layer and a batch normalization layer. This is followed by six repetitions of the Subnetwork Unit shown in Fig. S1(b), a ReLU activation layer, a 2D max pooling layer, an additional convolutional layer and batch normalization layer, and another six repetitions of the Subnetwork Unit. Finally, the network includes a ReLU layer, a dropout layer, a fully connected layer, a softmax layer, and a classification output layer. Each Subnetwork Unit contains two shortcut connections to enhance training stability and enable deep feature learning [40]. Using this network, the possible range of the average Young modulus of the input material is limited to one class from among 15 classes.

In the second stage, the regression model is applied to a subset of data consisting of the class with the highest classification probability and its two adjacent classes (one before and one after). The regression task aims to output the five independent elastic constants $C_{ij}$ for the input material. For this purpose, a 194-layer CNN-based regression network was constructed as illustrated in Fig. S2, which allows high-precision prediction using the reduced dataset by the first-stage classification.

Using the developed deep-learning scheme, we predicted the elastic constants of the 42 existing hexagonal materials by inputing their elasticity images, which were created from resonant frequencies calculated by the Ritz method using the true elastic constants. (Because the measurement accuracy and the calculation accuracy with the Ritz method for the resonant frequencies are extremely high in usual RUS methods, it is reasonable to simulate the experiments with the calculated resonant frequencies.) Fig. 3 shows the prediction errors, defined as $(C_{pred} - C_{true})/C_{true}$. Despite the fact that the input elasticity images

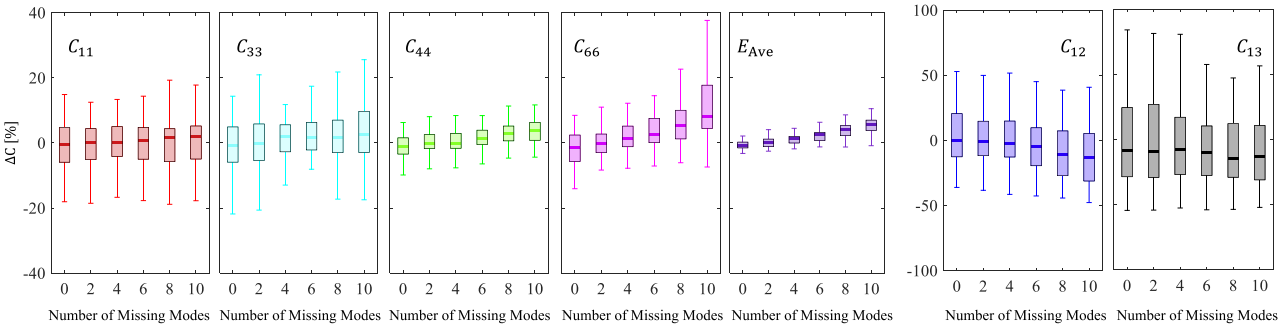


**Fig. 3.** Box plots for prediction accuracy for various elastic constants for the 42 existing hexagonal materials shown in Table S1. Horizontal axis denotes the number of missing modes involved in the input elasticity image.

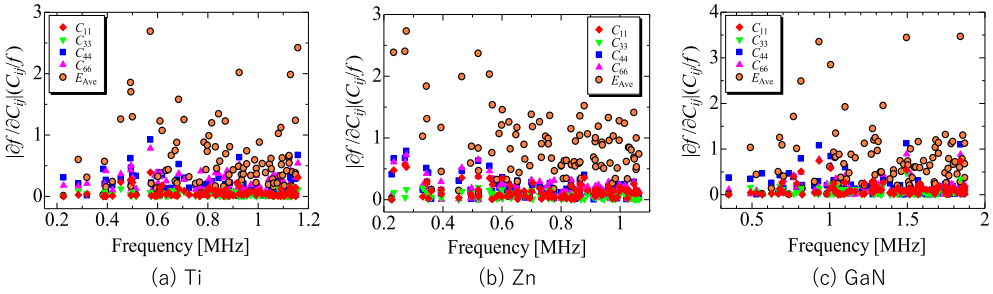


**Fig. 4.** Contributions of principal elastic constants to resonant frequencies for (a)Ti, (b)Zn, and (c)GaN specimens with the reference size.

were untrained (not included in the dataset), our DL scheme allows high-accurate prediction of the elastic constants; the average prediction errors for the diagonal components $C_{11}$, $C_{33}$, $C_{44}$, and $C_{66}$ are approximately 5 %, and the error in the average Young modulus is about 1.5 %. The prediction accuracy for the off-diagonal components $C_{12}$ and $C_{13}$ is, however, lower. This is expected because their contributions to the resonance frequencies are smaller. In fact, in the RUS method, the determination accuracy for the off-diagonal components is generally lower.

The developed CNNs also demonstrate strong robustness to the missing resonance modes. In RUS experiments, we sometimes fail to detect a few resonant modes when the transducer contacts near the nodal points. Such a missing mode makes the mode-identification procedure highly complicated. On the other hand, a missing mode only blackens one pixel among 900 pixels in each layer, and it less affects the elasticity image. Actually, when more than six modes were missing, exceeding the maximum number considered in the training dataset, the prediction accuracy remains nearly unaffected. As the number of missing modes increases, the diagonal elastic constants and the average Young modulus are slightly overestimated. This is attributed to the sparsity in the elasticity image caused by missing pixels, which led the network to infer a stiffer material.

We here discuss the significance of the average Young modulus for successful prediction achieved in this study. There are two typical relationships between the elastic constants of a single crystal and its macroscopically isotropic aggregate. One is the Voigt relationship under uniform strain throughout the aggregate. The resultant averaged bulk modulus $B^V_{\mathrm{Ave}}$ and averaged shear modulus $G^V_{\mathrm{Ave}}$ are given as follows for hexagonal materials.

$$B^V_{\mathrm{Ave}} = \frac{1}{9}\left[2C_{11} + C_{33} + 2\left(C_{12} + 2C_{13}\right)\right],$$

$$G^V_{\mathrm{Ave}} = \frac{1}{15}\left[2C_{11} + C_{33} - \left(C_{12} + 2C_{13}\right) + 3\left(2C_{44} + \frac{C_{11} - C_{12}}{2}\right)\right].$$

The other is the Reuss relationship under the uniform stress, yeilding

$$B^R_{\mathrm{Ave}} = \left[2s_{11} + s_{33} + 2\left(s_{12} + 2s_{13}\right)\right]^{-1},$$

$$G^R_{\mathrm{Ave}} = 15\left[8s_{11} + 4s_{33} - \left(4s_{12} + 8s_{13}\right) + 6\left(s_{44} + s_{11} - s_{12}\right)\right]^{-1}.$$

Here, $s_{ij}$ denote the compliance-matrix components of the hexagonal crystal. Since the true moduli are expected to lie between Voigt and Reuss values [41], Hill simply averaged them (called Hill approximation) as $B^H_{\mathrm{Ave}} = (B^V_{\mathrm{Ave}} + B^R_{\mathrm{Ave}})/2$ and $G^H_{\mathrm{Ave}} = (G^V_{\mathrm{Ave}} + G^R_{\mathrm{Ave}})/2$. Using the Hill approximation, we deduced the average Young modulus as

$$E_{\mathrm{Ave}} = \frac{9B^H_{\mathrm{Ave}}G^H_{\mathrm{Ave}}}{3B^H_{\mathrm{Ave}} + G^H_{\mathrm{Ave}}}. \tag{5}$$

We find that $E_{\mathrm{Ave}}$ most contributes to the free-vibration resonant frequencies of a solid among various elastic constants. Fig. 4 shows contribution values of principal elastic constants, including $E_{\mathrm{Ave}}$, for three representative hexagonal materials. It is clearly seen that the contribution value of $E_{\mathrm{Ave}}$ is significantly larger than those of other elastic constants by a factor of ~10. This finding indicates that when we understand a resonant spectrum as a group of resonance frequencies rather than individually, the average Young modulus governs it most strongly, and the elasticity image that expresses the overall properties of the resonance behavior most strongly depends on the average Young modulus. Therefore, the classification strategy based on the average Young modulus is highly reasonable.

Next, we discuss the frequency resolution in the elasticity image. We created the elasticity image by dividing the prescribed range of the elasticity parameter into 900 discrete segments, corresponding to a frequency resolution in the kHz range. In contrast, the measurement error of the resonant frequency is typically less than 0.001 % or in the Hz order in the RUS method [42], and one may want to divide the elasticity parameter much more finely to maintain the high frequency resolution of the measurement. However, we intentionally adopt the much lower frequency resolution (kHz order) because the reduction in the resolution minimizes various influences caused by errors in dimensions, orientation, mass density and so on. For example, a 0.2 % dimension error would cause less than ~1-kHz frequency error, which will not affect the elasticity image significantly. Therefore, the resolution in the elas-

**Table 1**
Elastic constants of rotus-type porous copper and unidirectionally fiber reinforced composites.

| | Porous(17 %) | | Porous(31 %) | | B-Al comp. | | | | SiC-Ti comp. | | | |
|---|---|---|---|---|---|---|---|---|---|---|---|---|
| | Experiment [15] | Present | Experiment [15] | Present | Experiment [13] | Present[a] | Experiment[b] | Present[c] | Experiment [14] | Present[a] | Experiment[b] | Present[c] |
| $C_{11}$ | 128.85 | 110.21 | 59.69 | 59.53 | 185.9 | 236.78 | 182.6 | 179.66 | 189.6 | 217.54 | 188.6 | 182.11 |
| $C_{33}$ | 148.62 | 131.92 | 78.08 | 77.66 | 246.1 | 290.24 | 246.1 | 231.11 | 246.7 | 292.50 | 246.7 | 237.99 |
| $C_{44}$ | 35.04 | 32.93 | 33.99 | 36.22 | 55.1 | 55.37 | 55.4 | 53.90 | 56.86 | 56.86 | 56.41 | 54.10 |
| $C_{66}$ | 25.81 | 26.73 | 16.04 | 15.86 | 50.8 | 52.07 | 52.8 | 51.30 | 54.16 | 52.7 | 55.60 | 55.5 |
| $E_{Ave}$ | 76.60 | 75.03 | 55.98 | 56.80 | 151.14 | 154.73 | 151.14 | 148.07 | 154.35 | 157.60 | 154.35 | 150.20 |
| $C_{12}$ | 77.24 | 56.76 | 27.60 | 27.81 | 74.9 | 132.63 | 76.99 | 77.09 | 75.82 | 112.15 | 77.34 | 71.21 |
| $C_{13}$ | 94.74 | 75.03 | 36.20 | 36.79 | 60.3 | 125.11 | 59.85 | 42.67 | 69.96 | 105.17 | 67.75 | 63.37 |
| $C_{22}$ | | | | | 183.5 | | | | 190.6 | | | |
| $C_{55}$ | | | | | 55.8 | | | | 55.96 | | | |
| $C_{23}$ | | | | | 59.4 | | | | 65.53 | | | |

[a] Predicted values from resonant frequencies calculated under orthorhombic symmetry.
[b] Elastic constants obtained by approximating the orthorhombic system as a hexagonal system.
[c] Predicted values from resonant frequencies calculated under hexagonal symmetry.

ticity parameter is a key for making the CNN tolerant to various error factors.

We also emphasize the important advantage of our DL approach that we can use many resonant frequencies up to 100. In conventional RUS methods, it is usually possible to measure more than 100 resonant frequencies, but because of the extreme difficulty in mode identification on such higher frequencies, we cannot use them in the inverse calculation. Conversely, because mode identification is unnecessary in creating the elasticity image, such high-frequency modes can be involved and crucial in the elasticity image.

As discussed in the introduction, even materials that are not strictly hexagonal symmetry can often be approximated as hexagonal when they exhibit near-transverse isotropy. Based on this, we investigate whether the developed DL method is applicable to three composites: (i) a B-Al composite consisting of an aluminum matrix unidirectionally reinforced with boron fibers, showing orthorhombic symmetry [13]. (ii) SiC-Ti composites in which a matrix titanium alloy is reinforced with silicon carbide fibers, also showing orthorhombic symmetry [14], and (iii) lotus-type porous coppers with unidirectionally aligned voids resembling the structure of lotus roots [15]. The resonance spectra used for prediction are theoretically computed from the reported elastic constants show in Table 1 for each material.

The elastic constants predicted by our DL method are compared with experiments in Table 1 and Fig. 5. Concerning the porous coppers, the prediction accuracy remains higher, while the two composite materials exhibit larger prediction errors. This is likely due to the fact that these composites exhibit orthorhombic symmetry, whose spectral features cannot be fully captured by a network trained solely on hexagonal symmetry data. We then averaged the experimentally determined elastic constants around the longitudinal axis of the fibers and derived the elastic constants of hexagonal symmetry. This hexagonal approximation improved the prediction accuracy, demonstrating that our DL method can accurately predict elastic constants even for materials with heterogeneous and complex structures when they macroscopically exhibit hexagonal symmetry.

In this study, we have establish a deep-learning method for directly determining the five independent elastic constants of hexagonal crystals from resonance spectra, without relying on inverse calculation. To efficiently constrain the area for training data generation, we devise a new constraint diagram for hexagonal elastic constants, inspired by the classical Blackman diagram for cubic crystals. This is made possible by using the average Young modulus, which most strongly affects the overall resonant spectrum. Based on this, we constructed the two-step deep learning framework: the first classification network coarsely predicts the average Young modulus from the elasticity image created from the resonance spectrum. The second regression network then infers the full set of elastic constants using the dataset around the class identified by the first step.

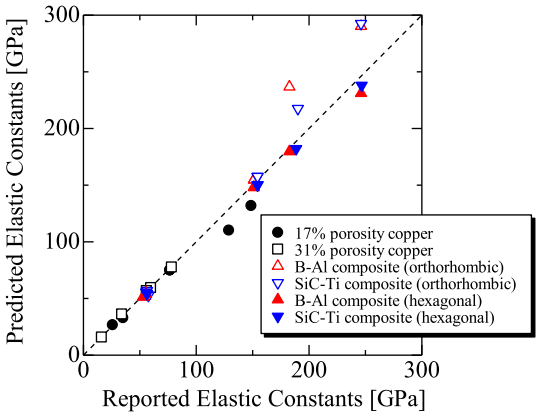


**Fig. 5.** Comparison between reported and predicted elastic constants for composite materials for the principal components.

This approach achieved high prediction accuracy; the prediction errors were ~5 % for principal diagonal elastic constants and 1.5 % for the average Young modulus, even with the presence of the missing resonance modes. Furthermore, its applicability was confirmed for composite materials that are approximately hexagonal symmetry, indicating its potential for practical use.

## CRediT authorship contribution statement

**Kazuya Kohira:** Data curation, Formal analysis, Investigation, Writing – original draft; **Shota Nakamura:** Data curation, Formal analysis, Investigation; **Hiroki Fukuda:** Formal analysis, Investigation, Methodology; **Kazuhiro Kyotani:** Formal analysis, Investigation; **Hirotsugu Ogi:** Conceptualization, Data curation, Formal analysis, Funding acquisition, Investigation, Methodology, Project administration, Software, Supervision, Validation, Visualization, Writing – original draft, Writing – review & editing.

## Declaration of competing interest

The authors declare that they have no known competing financial interests or personal relationships that could have appeared to influence the work reported in this paper.

## Supplementary material

Supplementary material associated with this article can be found, in the online version at 10.1016/j.scriptamat.2025.117115.

- Supplementary Information:
  - Supplementary Table S1 shows reported and predicted elastic constants of 42 materials.
  - Supplementary Figures S1 and S2 show CNNs for classification and regression, respectively.
- WEB page for predicting five elastic constants of hexagonal materials through the DL method developed here: https://insightkk.net/web_app/CijPredict/

## References


[1] K. Kim, W.R.L. Lambrecht, B. Segall, Elastic constants and related properties of tetrahedrally bonded BN, AlN, GaN, and InN, Phys. Rev. B 53 (1996) 16310.
[2] A.F. Wright, Elastic properties of zinc-blende and wurtzite AlN, GaN, and InN, J. Appl. Phys. 82 (1997) 2833.
[3] P. Ravindran, L. Fast, P.A. Korzhavyi, B. Johansson, J. Wills, O. Eriksson, Density functional theory for calculation of elastic properties of orthorhombic crystals: application to $TiSi_2$, J. Appl. Phys. 84 (1998) 4891.
[4] S. Lebègue, J. Harl, T. Gould, J.G. Ángyán, G. Kresse, J.F. Dobson, Cohesive properties and asymptotics of the dispersion interaction in graphite by the random phase approximation, Phys. Rev. Lett. 105 (2010) 196401.
[5] A. Nagakubo, H. Ogi, H. Sumiya, K. Kusakabe, M. Hirao, Elastic constants of cubic and wurtzite boron nitrides, Appl. Phys. Lett. 102 (2013) 241909.
[6] K. Kusakabe, A. Wake, A. Nagakubo, K. Murashima, M. Murakami, K. Adachi, H. Ogi, Interplanar stiffness in defect-free monocrystalline graphite, Phys. Rev. Mater. 4 (2020) 043603.
[7] T. Oka, Recent development of vertical GaN power devices, Jpn. J. Appl. Phys. 58 (SB0805) (2019).
[8] F. Roccaforte, P. Fiorenza, G. Greco, R.L. Nigro, F. Giannazzo, F. Iucolano, M. Saggio, Emerging trends in wide band gap semiconductors (SiC and GaN) technology for power devices Microelectron. Eng. 187 (2018) 66.
[9] J. Wadsworth, F.H. Froes, Developments in metallic materials for aerospace applications„ JOM 41 (1989) 12.
[10] S.K. Hyun, K. Murakami, H. Nakajima, Anisotropic mechanical properties of porous copper fabricated by unidirectional solidification, Mater. Sci. Eng. A 299 (2001) 241.
[11] S. Yamamura, H. Shiota, K. Murakami, H. Nakajima, Evaluation of porosity in porous copper fabricated by unidirectional solidification under pressurized hydrogen, Mater. Sci. Eng. A 318 (2001) 137.
[12] J.Y. Rho, L. Kuhn-Spearing, P. Zioupos, Mechanical properties and the hierarchical structure of bone, Med. Eng. Phys. 20 (1998) 92.
[13] H. Ledbetter, C. Fortunko, P. Heyliger, Orthotropic elastic constants of a boron-aluminum fiber reinforced composite: an acoustic resonance spectroscopy study, J. Appl. Phys. 78 (1995) 1542.
[14] H. Ogi, M.L. Dunn, K. Takashima, H. Ledbetter, Elastic properties of a unidirectional SiCf/Ti composite: acoustic-resonance measurements and micromechanics predictions, J. Appl. Phys. 87 (2000) 2769.
[15] T. Ichitsubo, M. Tane, H. Ogi, M. Hirao, T. Ikeda, H. Nakajima, Anisotropic elastic constants of lotus-type porous copper: measurements and micromechanics modeling, Acta Mater. 50 (2002) 4105.
[16] S. Bernard, Q. Grimal, P. Laugier, Accurate measurement of cortical bone elasticity tensor with resonant ultrasound spectroscopy, J. Mech. Behav. Biomed. Mater 18 (2013) 12.
[17] G.A. Alers, J.R. Neighbours, The elastic constants of zinc between 4.2° and 670° K, J. Phys. Chem. Solid. 7 (1958) 58.
[18] D.I. Bolef, N.T. Melamed, M. Menes, Elastic constants of hexagonal cadmium sulfide, J. Phys. Chem. Solid. 17 (1960) 143.
[19] J.B. Wachtman, W.E. Tefft, D.G. Lam, R.P. Stinchfield, Rectangular Parallelepiped Resonance Method for Piezoelectric Crystals and Elastic Constants of Alpha-Quartz, 1960, p. 213.
[20] H.H. Demarest, Cube resonance method to determine the elastic constants of solids, J. Acoust. Soc. Am. 49 (1971) 768.
[21] I. Ohno, Free vibration of a rectangular parallelepiped crystal and its application to determination of elastic constants of orthorhombic crystals, J. Phys. Earth 24 (1976) 355.
[22] I. Ohno, Rectangular parallelepiped resonance method for piezoelectric crystals and elastic constants of alpha-quartz, Phys. Chem. Miner. 17 (1990) 371.
[23] W. Visscher, A. Migliori, T. Bell, R. Reinert, On the normal modes of free vibration of inhomogeneous and anisotropic elastic objects, J. Acoust. Soc. Am. 90 (1991) 2154.
[24] P. Heyliger, A. Jilani, The free vibrations of inhomogeneous elastic cylinders and spheres, Int. J. Solid. Struct. 29 (1992) 2689.
[25] J. Maynard, The use of piezoelectric film and ultrasound resonance to determine the complete elastic tensor in one measurement, J. Acoust. Soc. Am. 91 (1992) 1754.
[26] A. Migliori, J.L. Sarrao, W.M. Visscher, T.M. Bell, M. Lei, Z. Fisk, R.G. Leisure, Resonant ultrasound spectroscopic techniques for measurement of the elastic moduli of solids, Physica B 183 (1993) 1.
[27] J. Maynard, Resonant ultrasound spectroscopy, Phys. Today 49 (1996) 26.
[28] H. Ogi, H. Ledbetter, S. Kim, M. Hirao, Contactless mode-selective resonance ultrasound spectroscopy: electromagnetic acoustic resonance, J. Acoust. Soc. Am. 106 (1999) 660.
[29] H. Ogi, S. Kai, H. Ledbetter, R. Tarumi, M. Hirao, K. Takashima, Titanium's high-temperature elastic constants through the hcp-bcc phase transformation, Acta Mater. 52 (2004) 2075.
[30] H. Ogi, K. Sato, T. Asada, M. Hirao, Complete mode identification for resonance ultrasound spectroscopy, J. Acoust. Soc. Am. 112 (2002) 2553.
[31] H. Ogi, M. Fukunaga, M. Hirao, H. Ledbetter, Elastic constants, internal friction, and piezoelectric coefficient of $\alpha$-$TeO_2$, Phys. Rev. B 69 (2004) 024104.
[32] K. Adachi, H. Ogi, N. Takeuchi, N. Nakamura, H. Watanabe, T. Ito, Y. Ozaki, Unusual elasticity of monoclinic $\beta$-$Ga_2O_3$, J. Appl. Phys. 124 (2018) 085102.
[33] S. Bernard, G. Marrelec, P. Laugier, Q, Bayesian normal modes identification and estimation of elastic coefficients in resonant ultrasound spectroscopy, Invers. Probl. 31 (2015) 065010.
[34] T. Li, Z. Zhao, C. Sun, L. Cheng, X. Chen, R. Yan, R.X. Gao, WaveletKernelNet: an interpretable deep neural network for industrial intelligent diagnosis, IEEE Trans. Syst. Man Cybern. Syst. 52 (2022) 2302.
[35] Z. Hou, J. Liu, S. Yu, Enhanced analog circuit fault diagnosis via continuous wavelet transform and dual-stream convolutional fusion, Sci. Rep. 15 (2025).
[36] H. Ren, Q. Zhang, Z. Wang, G. Zhang, H. Liu, W. Guo, S. Mukamel, J. Jiang, Machine learning recognition of protein secondary structures based on two-dimensional spectroscopic descriptors, Proc. Natl. Acad. Sci. U.S.A. 119 (2022) 2202713119.
[37] H. Fukuda, A. Nagakubo, O.B. Wright, K. Kyotani, H. Ogi, Deep-learning-assisted resonant ultrasound spectroscopy for cubic solids, Phys. Rev. Appl. 20 (2023) 034048.
[38] M. Blackman, On anomalous vibrational spectra, Proc. R. Soc. Lond. A 164 (1938) 62.
[39] H.M. Ledbetter, Blackman Diagrams and Elastic-Constant Systematics, II of *San Diego*, Academic Press, 2001.
[40] K. He, X. Zhang, S. Ren, J. Sun, Deep residual learning for image recognition, in: Proc. IEEE Conf. Comput. Vis. Pattern Recognit, IEEE Conf. Comput. Vis. Pattern Recognit, 2016, p. 770.
[41] R. Hill, The elastic behaviour of a crystalline aggregate, Proc. Phys. Soc. A 65 (1952) 349.
[42] H. Ogi, T. Ohmori, N. Nakamura, M. Hirao, Elastic, anelastic, and piezoelectric coefficients of $\alpha$-quartz determined by resonance ultrasound spectroscopy, J. Appl. Phys. 100 (2006) 053511.